# BL22XU
# JAEA Actinide Science I

## 1. Introduction

BL22XU was constructed as a hard X-ray undulator beamline extending from the Storage Ring building to the RI Laboratory, and has been operational since May 2002 as a supplementary beamline to the soft X-ray undulator beamlines BL23SU. In accordance with the new vision of JAEA, which is "A new future pioneered by the synergy of nuclear and renewable energies," the following research and development activities are currently underway: "Synergy: R&D for pursuing the synergy of nuclear and renewable energies," "Sustainable: R&D for making nuclear energy itself sustainable," and "Ubiquitous: R&D for applying nuclear technology widely to society, not limited to the energy field."

In September 2022, the utilization of a restricted amount of sealed nuclear fuel material was authorized, with operations scheduled to begin in September 2023. Subsequently, from January to February 2024, measurements were conducted on radioactive particles containing nuclear fuel that had been collected from within the containment vessel of Unit 2 at the Fukushima Daiichi Nuclear Power Station. Simultaneous measurements within the same field of view were performed by microbeam X-ray fluorescence analysis (XRF), X-ray diffraction (XRD), and X-ray absorption spectroscopy (XAFS). In July 2024, measurements of radioactive particles were conducted for Units 1 through 3. In November 2024, the initial trial removal of fuel debris samples from Unit 2 was conducted, and in January and February 2025, the world's first successful synchrotron radiation analysis experiment was performed.

BL22XU has two double-crystal monochromators. One is a single-cam-type monochromator with a multicrystal switching system. This monochromator can utilize wide-energy-range X-rays from 4 to 72 keV by using Si(111) and Si(311) crystals. The other is a calculation-and-combination-type monochromator. This monochromator can utilize high-flux X-rays from 35 to 70 keV by employing Si(111) crystals.

BL22XU has mirrors for focusing and higher harmonics rejection. The mirrors focus X-rays of 1 mm height and 3 mm width to 0.2 and 0.4 mm, respectively, in the RI Laboratory at 120 m from the light source. The three mirrors are switched to reject harmonics higher than 7, 16, and 30 keV. A beryllium diffraction lens system for high energy and a Kirkpatrick–Baez (KB) micro-focusing system for less than 40 keV are also used, enabling experiments with beam sizes of 1 $\mu m^2$ or smaller.

## 2. Experimental Hutch 1 (EH1)

### 2-1. Large diffractometer

The Bragg coherent X-ray diffraction imaging (Bragg-CDI) apparatus at EH1 of BL22XU continues to support advanced studies of nanoscale crystalline particles. In 2024, Bragg-CDI was utilized to visualize lattice strain in hydrogen-rich perovskite oxyhydrides synthesized via mechanochemical methods [1]. These materials, such as $BaTiO_{3-x}H_x$ with $x$ approaching 1, exhibited significantly enhanced catalytic activity for ammonia synthesis compared with topochemically prepared counterparts. The imaging revealed nonnegligible lattice strain not only at the surface

but also within the crystal, suggesting that strain-induced effects contribute to the improved functionality of $H^-$-based materials.

In parallel, Bragg-CDI as well as synchrotron X-ray diffraction were applied to investigate strain gradients across heteroepitaxial interfaces in $BaTiO_3/KNbO_3$ core–shell nanocomposite particles [2]. The results revealed that more than 60% of the particle volume was occupied by structure gradient regions (SGRs), which expanded significantly with decreasing temperature and reduced core size. These findings demonstrate that nanoscale interface engineering can effectively tailor dielectric properties by promoting polarization rotation and domain complexity.

Additionally, the self-assembly of oblique stripe 90° polarization domains in relaxor ferroelectrics $Pb(Mg_{1/3}Nb_{2/3})_{0.722}Ti_{0.278}O_3$ was investigated [3]. The evolution of mesoscopic polarization structures was observed under near thermal equilibrium conditions, revealing domain formation driven by the balance between dipole–dipole and elastic free energies.

### 2-2. Diamond-anvil-cell diffractometer

The diamond-anvil-cell (DAC) diffractometer was designed for X-ray diffraction experiments under high pressure. Equipped large-area two-dimensional detectors cover a wide diffraction angle. Recently, not only structural studies under high pressure using DACs [4] but also many local structural studies by atomic pair-distribution function (PDF) analyses [5–9] have been conducted. By using the large-area flat detector and high-energy monochromatic X-rays up to 70 keV, we can measure X-ray total scattering patterns, which transform into PDFs, even in a high-$Q$ range with a short exposure time. Our rapid-acquisition PDF measurement system has been applied to a wide variety of functional materials, such as hydrogen-absorbing materials [5], metal-organic frameworks for catalysts [6], water clusters [7] and cement materials [8,9].

In FY2024, the flat panel detector that was newly installed began full-scale operation. This detector has the same detection area as the previous model, but the pixel size is 100 × 100 μm, which is one-quarter of the previous model (200 × 200 μm). Thus, this detector enables us to measure X-ray total scattering patterns with high angular resolution and can be applied to precise structural analysis by the X-ray diffraction of crystalline samples.

## 3. Experimental Hutch 3 (EH3)

### 3-1. Hard X-ray photoemission spectroscopy (HAXPES)

At the HAXPES station of BL22XU, the chemical state of Sn dopants in β-$Ga_2O_3$(001) single crystals was investigated by hard X-ray photoelectron spectroscopy (HAXPES). The Sn $2p_{3/2}$ spectrum exhibited a single sharp peak, clearly indicating that all dopant atoms occupy a unique chemical state. By direct comparison with reference spectra of Sn metal, SnO, and $SnO_2$, the binding energy of the dopant peak was assigned to an oxidized state, and the Sn dopant was identified as tetravalent $Sn^{4+}$ [1].

The high photon energy and bulk sensitivity of HAXPES were crucial for detecting the weak Sn $2p_{3/2}$ signal from the doped crystal, which could not be reliably obtained by conventional laboratory-based XPS. Complementary XANES and EXAFS measurements confirmed that Sn occupies the Ga octahedral substitutional site, accompanied by a slightly increased Sn–O bond length owing to local

lattice relaxation [10].

These results demonstrate that the BL22XU HAXPES station can be used to determine the electronic state of dilute dopants in functional oxides. Establishing that electrically active Sn dopants in β-$Ga_2O_3$ are stabilized as $Sn^{4+}$ at octahedral Ga sites provides critical insight into carrier control and resistivity engineering in ultrawide-bandgap semiconductor devices.

### 3-2. X-ray absorption fine structure (XAFS)

#### (1) XAFS and XRD structural analysis of ultrahigh-temperature melted oxides

The melting points of $UO_2$ and $ZrO_2$ are exceptionally high, which complicates their sustained maintenance in a molten state. Consequently, in this study, the gas levitation method was utilized. This technique involves the levitation of a minute sample with an approximate diameter of 1 mm, using a gas flow, and the subsequent heating of the sample to its molten state via laser irradiation. The employment of gas levitation technology in the execution of XAFS and XRD measurements on levitated molten $UO_2$ and $ZrO_2$ is anticipated to yield substantial data, thereby facilitating a comprehensive discussion on the material properties of local structure.

In order to conduct synchrotron radiation experiments using internationally regulated materials such as $UO_2$ at SPring-8, triple sealing is required. The first seal is the gas levitation apparatus, the second is the glove box, and the third is the experimental hutch. Consequently, the gas levitation apparatus must be installed inside the glove box.

The experiment was conducted after installing a custom-built gas-floating melting apparatus inside the synchrotron radiation glove box located at BL22XU. Ionization chambers, utilized for the measurement of transmitted X-ray intensity, were positioned in front of and behind the glove box. A two-dimensional detector for X-ray scattering measurements was positioned at an angle of approximately 30 degrees diagonally forward. A 19-element Ge semiconductor detector (SSD) or a silicon drift detector (SDD) was positioned at a 90-degree direction to the incident X-ray, enabling the simultaneous measurement of XAFS and XRD spectra in a short time.

XAFS and XRD measurements of $UO_2$ were performed at room temperature. The EXAFS spectrum clearly confirmed the correlation between the nearest-neighbor U–O and second-nearest-neighbor U–U bonds. The XRD pattern also clearly showed a cubic crystal diffraction pattern. Furthermore, heating experiments on $UO_2$ were conducted. Camera images confirmed that $UO_2$ reached a molten state. However, to measure molten $UO_2$, conditions enabling a more stable suspension than previously achieved must be identified.

Fig. 1. Gas levitation system in the glove box at the BL22XU experimental hutch.

**(2) High-energy-resolution fluorescence detection (HERFD) XAFS**

A proven portable crystal spectrometer from the JASRI beamline will be brought into the sealed small-quantity nuclear fuel permit facility, EH3 in the RI Building, to develop the technology for applying the spectrometer to contaminants originating from the Fukushima Daiichi Nuclear Power Plant and future debris samples. The current evaluations will utilize samples of U and U, whose absorption edges have been determined to approximate those of the U sample, or Zr. The assessment will encompass the evaluation of signal intensity and the determination of its sufficiency. Additionally, the feasibility of measuring XANES spectra to facilitate valence state evaluation in dilute samples or in the presence of interfering coexisting elements will be ascertained. This will lay the foundation for subsequent measurements of U and Pu.

A microbeam system equipped with a KB mirror was installed on a 1 m × 1.5 m XAFS experimental table. The beam was focused to approximately 1 $\mu m^2$ at 18–20 keV and then irradiated onto a sample placed at the focal point 500 mm downstream from the lower edge of the mirror. The X-ray fluorescence from the sample was spectroscopically analyzed using a crystal spectrometer positioned downstream of the baseplate and detected using a two-dimensional detector, PILATUS 100K. The diffraction crystals and angles utilized were Ge 993 for the Y Kα1 line and InSb 999 for the Zr Kα1 line. The chamber of the crystal spectrometer was purged with He to minimize the absorption and scattering of the fluorescent X-rays from the sample, and the X-rays were spectroscopically dispersed by the crystal in air. The sample consisted of pellets prepared using Zr metal foil and pellets for transmission method standards made by diluting $Y_2O_3$ and $ZrO_2$ powders with boron nitride.

Figure 2 shows the fluorescence spectra obtained using Amptek's FAST SDD silicon drift detector and the crystal spectrometer developed in this study. This crystal spectrometer enabled the acquisition of fluorescence spectra with a high energy resolution of approximately 0.2 eV. Figure 3 shows the XANES spectra measured simultaneously with the crystal spectrometer and SDD. The pre-edge structure of the XANES, which cannot be obtained with the SDD, was acquired within a measurement time of about 1 h.

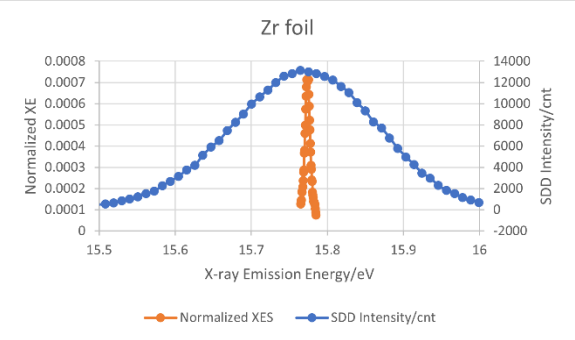


Fig. 2. Zr Kα fluorescence spectra obtained with SDD and crystal spectrometer.

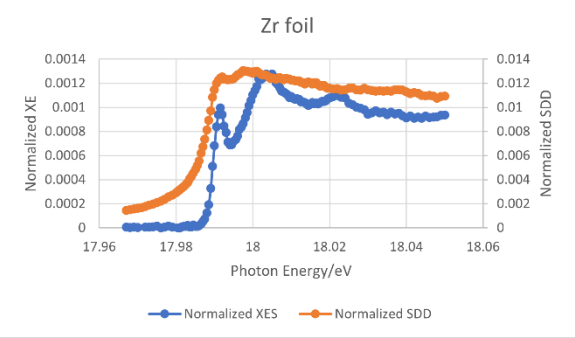


Fig. 3. SDD and HERFD-XANES for Zr K-edge XANES spectra.

### 3-3. Stress/imaging measurements

In this device, deformation and state changes inside a material are determined by a diffraction method and an imaging method using high-energy synchrotron radiation X-rays.

Figure 4 shows an XRD pattern of single-crystal $Yb_{0.148}Co_4Sb_{12.54}$. A single-crystal sample of $Yb_xCo_4Sb_{12}$ was grown by the Sb-flux method, employing high-purity Yb grains (99.9%, Rare Metallic Co., Japan), Co grains (99.97%, Rare Metallic Co., Japan), and Sb shots (99.9999%, Kojundo Chemical Co., Japan) as starting materials. An X-ray energy of 69.42 keV was used in this study. By stacking diffraction images via the tilting of the normal vector of {001}, a Laue pattern comprising individual Laue spots was clearly obtained, indicating uniform crystalline quality within the beam size of 2 × 0.2 × 0.2 mm during measurement. From the data of the identified (008) peak, the interplanar distance $d$ was determined. Under these conditions, the relationship between stress and strain under compression loading toward the {001} direction was observed. Figure 5 shows the stress–strain (S–S) curve of $Yb_{0.148}Co_4Sb_{12.54}$. Lattice strain $\varepsilon$ was calculated as

$$\varepsilon = \frac{d-d_0}{d_0},$$

where $d$ is the lattice spacing obtained from the (008) peak and $d_0$ is the (008) lattice spacing obtained in the absence of strain. It was observed that until the compressive strain exceeded 0.07%, the approximation did not properly align with the S–S curve. However, in the compressive strain range from 0.07 to 0.2%, the curve exhibited a nearly constant slope before reaching the yield limit. This linear relationship in the S–S curve indicates that the single crystal of SKD can deform elastically in this strain range. The slope in the S–S linear relationship, known as Young's modulus $E$, was determined to be 154.6 GPa, which closely corresponds to reported experimental values of polycrystalline $CoSb_3$ [11].

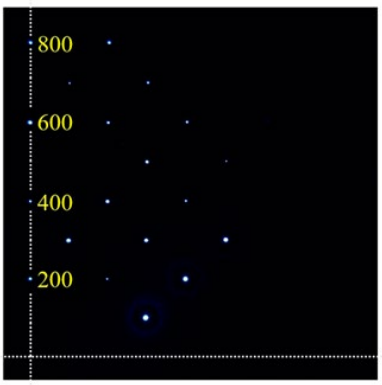


Fig. 4. XRD pattern of single-crystal

$Yb_{0.148}Co_4Sb_{12.54}$.

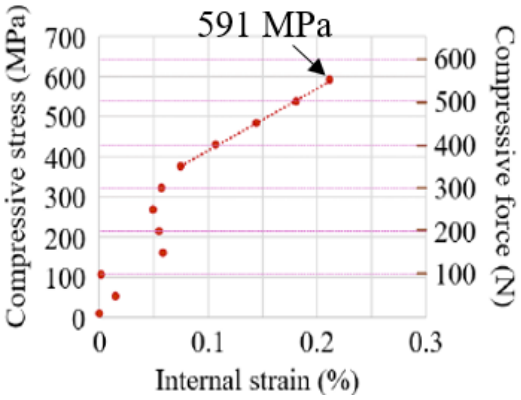


Fig. 5. Stress–strain curve of single crystal.

### 3-4. κ -type diffractometer

Crystal structure analysis using BL22XU and soft X-ray spectroscopy using BL23SU resulted in the following example. We present the experimental results for the niobium-based perovskites $NaNbO_3$, $AgNbO_3$, and $KNbO_3$ [12] as an example of research in which structural analysis and spectroscopic experiments are combined. Alkali metals, such as sodium (Na) and potassium (K), are highly ionic and were thought to be in a fully ionic state. However, as shown in Fig. 6, the absorption spectrum of Na obtained at BL23SU differed from that of the fully ionic compound NaF. A similar spectrum was observed in $Bi_{0.5}Na_{0.5}TiO_3$, indicating that it is in a hybridized state with the surrounding oxygen.

Furthermore, DFT calculations were performed to connect the structural analysis conducted at BL22XU with the spectroscopic experiments conducted at BL23SU. $AgNbO_3$ differs from $NaNbO_3$ and $KNbO_3$ in terms of its O K edge X-ray absorption spectrum near the Fermi energy. We calculated the oxygen partial density of states (PDOS) using the structure obtained from the experiment and compared it with the experimental data in Fig. 2. The peak positions of the spectrum are generally reproduced. Verifying the spectrum using DFT calculations effectively mitigates the bias of the rigid sphere model in structural analysis [13].

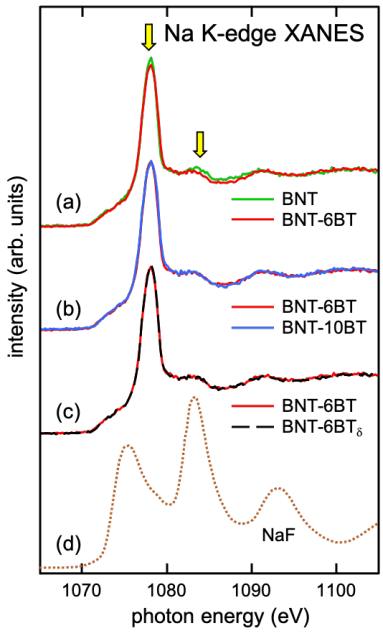


Fig. 6. Na K-edge absorption spectrum for $Bi_{0.5}Na_{0.5}TiO_3$ and $BaTiO_3$

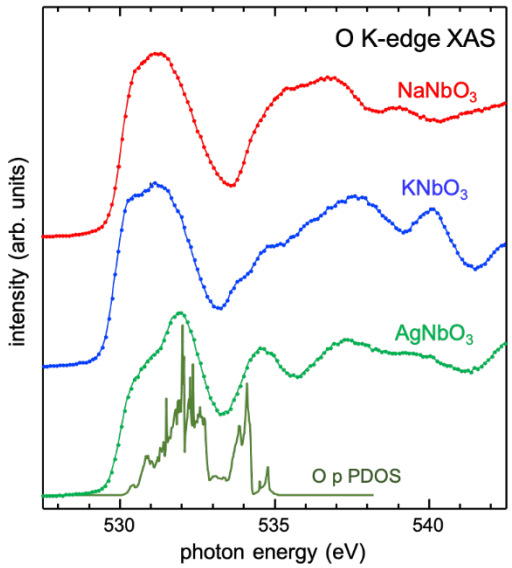


Fig. 7. O K-edge absorption spectrum of Nb-related perovskite oxides and result of DFT calculation for PDOS of $AgNbO_3$.

Author(s)
TANIDA Hajime[*1], OHWADA Kenji[*2], MACHIDA Akihiko[*2], KOBATA Masaaki[*1], SHOBU Takahisa[*1], YONEDA Yasuhiro[*1]

[*1]Japan Atomic Energy Agency
[*2]National Institutes for Quantum Science and Technology

References:

[1] Takeiri, F. *et al.* (2025). *J. Am. Chem. Soc.*, **147**, 24482–24490.
[2] Furukawa, R. *et al.* (2025). *Jpn. J. Appl. Phys.*, **64**, 08SP10.
[3] Namikawa, K. *et al.* (2024). *J. Phys. Chem. Solids.*, **192**, 112106.
[4] Chen, W.-T. *et al.* (2025). *Nat. Commun.* **16**, 2128.
[5] Asano K. *et al.* (2024). *ACS Appl. Energy Mater.* **7**, 11644–11651.
[6] Koh J. *et al.* (2024). *ACS Nano* **18**, 28986–28998.
[7] Sonobe K. *et al.* (2024). *ChemPhysChem* **25**, e202400583.
[8] Im S. *et al.* (2025). *Constr. Build. Mater.* **459**, 139742.
[9] Kim G. *et al.* (2025). *Cem. Concr. Compos.* **150**, 105562.
[10] Tsai, Y. *et al.* (2024). *Appl. Phys. Lett.* **124**, 112105.
[11] Nakasawa, H. *et al.* (2025). *J. Jpn. Soc. Powder Metallurgy* **72,** S997–S1001.
[12] Yoneda, Y Kobayashi, T. Tsuji, T. Matsumura, D. Saitoh, Y. & Noguchi, Y. (2023). *Jpn. J. Appl. Phys.* **62**, SM1006.
[13] Yoneda, Y. Kobayashi, T. Tsuji, T. Matsumura, D. Saitoh, Y & Noguchi, Y. (2024). *Jpn. J. Appl. Phys.* **63**, 09SP12.